Emulsions in homogeneous shear turbulence

By M. E. Rosti†, Z. Ge†, S. S. Jain, M. S. Dodd AND L. Brandt†‡

We simulate the flow of two immiscible and incompressible fluids in a homogeneous shear turbulent flow at a moderately high Reynolds number by using a volume of fluid method. The viscosity and density of the two fluids are equal, and various surface tensions and initial droplet diameters are considered. We show that the two-phase flow reaches a statistically steady state with reduced Reynolds numbers owing to the presence of the interface, which acts as a sink of turbulent kinetic energy for the solvent fluid.

1. Introduction

The understanding of turbulent two-phase flows with droplets or bubbles is important in many natural and industrial processes (e.g., rain formation, breaking ocean waves, spray cooling, and spray atomization in combustors). In these flows, the turbulence is altered directly by droplet feedback on the surrounding fluid and indirectly by droplet-droplet interactions. Note that, compared with solid particles, droplets can deform, develop internal circulation, break up, and coalesce with other droplets. Thus, complex mechanisms are expected to be active.

Direct numerical simulation (DNS) has become a crucial tool for understanding turbulence in two-phase flows, resolving the full range of temporal and spatial scales present in the flow at the continuum level (Balachandar & Eaton 2010). Depending on the relative size of the particle (D) to the smallest length scale in turbulence (η), spherical particles (or droplets) in isotropic turbulence can be broadly classified as sub-Kolmogorov ($D \ll \eta$) or finite size ($D > \eta$). Extensive studies have been conducted on turbulent flows laden with sub-Komogorov-size particles (Eaton & Fessler 1994; Ferrante & Elghobashi 2003; Sardina *et al.* 2012), characterizing the turbulence modulation as well as explaining their preferential accumulation in the local flow field. More recently, DNS of finite-size, non-deformable solid particles have been reported (Cate *et al.* 2004; Lucci *et al.* 2010; Picano *et al.* 2015), adding more physics and complexity owing to advanced numerical algorithms and the increasing computational power.

Closely related to our problem, Dodd & Ferrante (2016) performed DNS of decaying homogeneous isotropic turbulence (HIT) with finite-size, deformable droplets at 5% volume fraction, with an initial Taylor-scale Reynolds number $Re_\lambda = 83$. By varying the droplet Weber number on the basis of the rms velocity of turbulence, the droplet–to–carrier fluid density ratio, and the droplet–to–carrier fluid viscosity ratio, they showed that the presence of the droplets always enhances the decay rate of the turbulent kinetic energy (TKE). Furthermore, the deformation, breakup, or coalescence of the droplets introduces an additional term to the turbulent kinetic energy (TKE) equation – the power of the surface tension. Termed Ψ_σ by Dodd & Ferrante (2016), it describes the rate of

† Linné Flow Center, KTH Royal Institute of Technology, Sweden
‡ Department of Energy and Process Engineering, Norwegian University of Science and Technology (NTNU), Norway

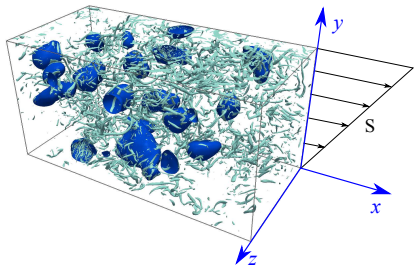

FIGURE 1. Sketch of the computational domain and of the Cartesian coordinate system.

change of the interfacial energy, balancing the energy transfer between the external fluid and the flow inside the droplets. Correct identification of these pathways for the TKE exchange is fundamental to understanding the tubulence modulation by the droplets.

Building upon previous studies, we consider finite-size bubbles/droplets of Taylor length scale in statistically stationary homogeneous shear turbulence (SS-HST) (Tavoularis & Corrsin 1981*a*,*b*; Pumir 1996; Sekimoto *et al.* 2016). HST flow is conceivably the simplest case in which the flow is not isotropic while remaining homogeneous in all spatial directions. Moreover, with a natural energy production mechanism, i.e., the shear, higher Reynolds numbers can be achieved relatively easily. We note that ideal HST is self-similar, implying an unbounded energy growth within infinite domains (Sukheswalla *et al.* 2013). This condition limits any numerical simulations to relatively short times concerning only the initial shearing of isotropic turbulence (Rogers & Moin 1987; Lee *et al.* 1990; Sukheswalla *et al.* 2013). However, as demonstrated by Pumir (1996) and Sekimoto *et al.* (2016), the finite computational box introduces a large-scale confinement effect similar to those enforced by the wall; thus, a meaningful statistically stationary state can be reached over long periods. These observations, combined with the insights recently gained in the droplet-turbulence interaction in HIT, motivate us to further investigate turbulence modulation due to droplets/bubbles in the SS-HST.

In this paper, we present DNS of the flow of two incompressible fluids separated by an interface. By changing the initial size of the dispersed phase and the Weber number, we aim to answer the following questions: (a) Can a statistically stationary state be reached when the suspended phase actively undergoes breakup and coalescence in HST?, (b) what determines the steady-state size distribution of the dispersed phase?, and (c) how does the dispersed phase change the TKE budget? HST shares many similarities with other shear flows (Sekimoto *et al.* 2016); therefore, by answering these questions, we expect to improve our understanding of the droplet-turbulence interaction and, hopefully, help future modelers gain intuition about more complex conditions.

This paper is organized as follows. In Section 2, we first discuss the flow configuration and the governing equations and then present the numerical methodology used to solve the problem. The results on the fully developed two-phase HST flow are presented in Section 3, where we answer the questions discussed above based on our observations. Finally, all the main findings and conclusions are summarized in Section 4.

2. Formulation

2.1. *Governing equations and numerical methods*

We consider the flow of two immiscible incompressible fluids in a periodic box subject to a uniform mean shear. Figure 1 shows a sketch of the geometry and the Cartesian

coordinate system, where x, y, and z (x_1, x_2, and x_3) denote the streamwise, shear, and spanwise coordinates, and u, v, and w (u_1, u_2, and u_3) denote the respective components of the velocity field. Standard periodic conditions are applied in x and z, and a shear-periodic boundary condition is enforced in y.

The total velocity field u_i can be decomposed for convenience into the sum of a mean component $\langle u_i \rangle_{xz}$ generated by the imposed shear S, i.e., $\langle u_i \rangle_{xz} = Sx_2\delta_{1i}$ where δ_{ij} is the Kronecker delta, and a fluctuating part u_i'. In this paper we indicate a spatial average in the x and z directions with $\langle \cdot \rangle_{xz}$, fluctuations with the prime symbol ($'$), and the average in the full volume with $\langle \cdot \rangle$. The time evolution of the fluctuating velocity u_i' is described by

$$\frac{\partial u_i'}{\partial t} + Sx_2\frac{\partial u_i'}{\partial x_1} + u_j'\frac{\partial u_i'}{\partial x_j} = -Su_2'\delta_{i1} - \frac{1}{\rho}\frac{\partial p}{\partial x_i} + \nu\frac{\partial^2 u_i'}{\partial x_j \partial x_j} + f_i \quad \text{and} \quad \frac{\partial u_i'}{\partial x_i} = 0, \quad (2.1)$$

where ρ and ν are the fluid density and kinematic viscosity, p is the pressure and f_i is the surface tension force defined as $f_i = \sigma\kappa n_i \delta$, where δ is the Dirac delta function at the interface, σ is the interfacial surface tension, κ is the interface curvature, and n_i is the normal to the interface. This equation is written in the so-called one-continuum formulation (Tryggvason *et al.* 2007) so that only one set of equations is solved in both phases. The problem is solved by introducing an indicator function H to identify each fluid phase so that $H = 1$ in the region occupied by the suspended fluid and $H = 0$ otherwise. Considering that both fluids are transported by the flow velocity, we update H in the Eulerian framework by the following advection equation written in divergence form, $\partial\phi/\partial t + \partial u_i H/\partial x_i = \phi \partial u_i/\partial x_i$, where ϕ is the cell-averaged value of the indicator function.

The above governing equations are solved numerically. First, the transport equation for ϕ is updated following the methodology described by Ii *et al.* (2012) and Rosti *et al.* (2018). Second, the momentum equation and incompressibility constraint are solved following the method proposed by Gerz *et al.* (1989) and recently adopted by Tanaka (2017), in which the second term on the left-hand side of the momentum equation, i.e., the advection due to the mean shear flow, is solved separately using a Fourier approximation. In particular, the second-order Adams–Bashforth method is applied for the convection and viscous terms in Eq. (2.1) to obtain an intermediate velocity $u_i'^{*} = u_i'^{n} + \Delta t\left(3/2\mathrm{rhs}^n - 1/2\mathrm{rhs}^{n-1}\right)$, where Δt is the time step from time t^n to t^{n+1} and $\mathrm{rhs} = -Su_2'\delta_{i1} - u_j'\partial u_i'/\partial x_j + \nu\partial^2 u_i'/\partial x_j \partial x_j$. The time step Δt is chosen such that the Courant–Friedrichs–Lewy (CFL) number $U_{max}\Delta t/\Delta x$ is smaller than unity, where $U_{max} = SL_y$, the maximum velocity of the mean shear flow inside the computational domain. The advection due to the mean shear flow is then solved separately using a Fourier approximation as $u_i'^{**}(x_1, x_2, x_3) = u_i'^{*}(x_1 - \Delta t S x_2, x_2, x_3)$. Note that Tanaka (2017) modified the approach of Gerz *et al.* (1989) by performing a similar additional step for the pressure. Our tests suggest that the original form by Gerz *et al.* (1989) is numerically more stable and physically consistent with the incompressibility constraint because the pressure is not a transported quantity. The surface tension term is then taken into account by updating the velocity field: we use the continuum surface force model by Brackbill *et al.* (1992) to compute the surface tension force where the normals are obtained with the usual Youngs approach (Youngs 1982), thus obtaining $u_i'^{***} = u_i'^{**} + \Delta t f_i^n$. Finally, we solve the Poisson's equation for the new pressure p^{n+1}

$$\frac{\partial^2 p^{n+1}}{\partial x_j \partial x_j} = \frac{\rho}{\Delta t}\frac{\partial u_i'^{***}}{\partial x_i}, \quad (2.2)$$

and correct the velocity with p^{n+1} to enforce the incompressibility constraint

$$u_i'^{n+1} = u_i'^{***} - \frac{\Delta t}{\rho}\frac{\partial p^{n+1}}{\partial x_i}. \tag{2.3}$$

The Poisson's equation, Eq. (2.2), is solved by exploiting the periodic and shear-periodic boundary conditions as detailed in Tanaka (2017).

2.2. *Setup*

The problem is governed by five dimensionless parameters, which are two aspect ratios of the computational domain (Sekimoto *et al.* 2016), $A_{xz} = L_x/L_z \approx 2.1$ and $A_{yz} = L_y/L_z \approx 1.1$; the Reynolds number based on the box width, $Re_z = SL_z^2/\nu = 15200$; the Weber number based on the initial droplet diameter D_0, $We_0 = \rho S^2 D_0^3/\sigma$; and the ratio of the initial droplet diameter to the box size $A_{Dz} = D_0/L_z$. In the following, we consider one case of single-phase flow as reference and nine cases of two-phase flows, as summarized in Table 1; in the multiphase cases, we vary the ratio A_{Dz} and We_0. Two other nondimensional parameters are the density and viscosity ratios, which are fixed to unity to study the separate effect of the Weber number (interfacial surface tension). Apart from the previous parameters based on geometrical dimensions and initial and boundary conditions, in the following discussion we use other nondimensional numbers that are more relevant to discuss the problem at hand, as representative of the solution itself, such as the Taylor microscale Reynolds number,

$$Re_\lambda = \left(\frac{2\mathcal{K}}{3}\right)^{1/2}\frac{\lambda}{\nu} = \left(\frac{5}{3\nu\varepsilon}\right)^{1/2} 2\mathcal{K}, \tag{2.4}$$

where λ is the Taylor microscale defined as $\sqrt{10\nu\mathcal{K}/\varepsilon}$ (Sekimoto *et al.* 2016), $\mathcal{K} = \langle u_i' u_i'\rangle/2$ is the TKE per unit mass, and $\varepsilon = \mu\langle \partial u_i'/\partial x_j \partial u_i'/\partial x_j\rangle$ is the dissipation rate of the fluctuating energy. Analogously, we define a Weber number based on λ

$$We_\lambda = \frac{\rho\left(2\mathcal{K} + S^2\lambda^2\right)\lambda}{\sigma}. \tag{2.5}$$

The choice of using λ in the definition of the Weber number instead of a dimension associated to the suspended phase is due to the fact that the interface is not only deforming, thus losing its original spherical shape, but also actively undergoing merging and breakup processes, which makes the definition of a unique dimension difficult. Therefore, we propose to rely on a fluid length scale, which, as shown below, successfully collapses most of our data.

3. Results

3.1. *Statistically stationary state*

We start our analysis by considering a single-phase flow at $Re_z \approx 15k$. The flow is initialized as a fully developed single-phase HIT, and at $t = 0$ the mean shear S is applied. As shown in Figure 2(a), once the shear is applied, the flow undergoes an initial transient characterized by a strong increase in the production of TKE, which is not in balance with the dissipation rate. After some time, however, the TKE $\mathcal{K}$ decreases owing to an increase in the dissipation, reaching a new statistically steady-state regime where, on average, the production balances the dissipation ($\mathcal{P}/\varepsilon = 1$). This state, called steady-state shear turbulence, was first found and characterized by Pumir (1996) and later

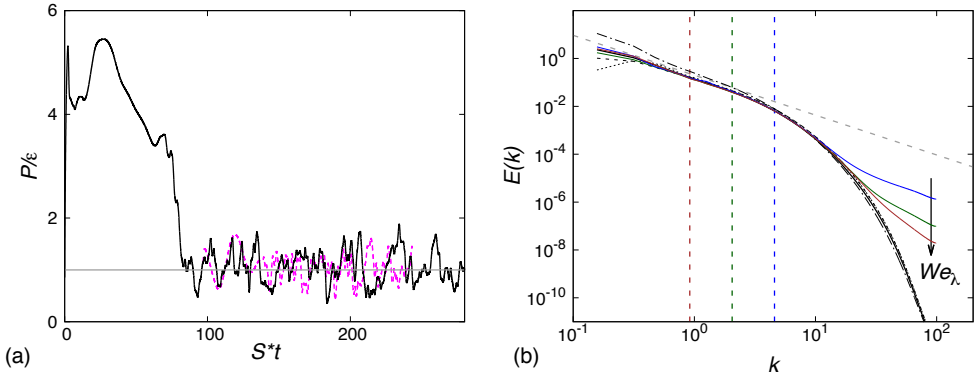

FIGURE 2. (a) Time history of the ratio between the turbulent production $\mathcal{P} = -\langle u'v'\rangle d\langle u\rangle/dy$ and the turbulent dissipation rate $\varepsilon = \mu\langle \partial u_i'/\partial x_j \partial u_i'/\partial x_j\rangle$. The solid and dashed lines represent the single and multiphase flows ($D_0 = 0.16L_z$ and $We_0 = 1$), respectively. (b) Spectra of the mean turbulent kinetic energy (solid line) and its three spatial components (dashed, dotted, and dashed-dotted lines) for the single-phase flow. The other three thin solid lines are used for the spectra of the two-phase flows with $We_0 = 2$, 4 and 10 and different initial diameters of the droplets, represented by the three vertical dashed lines. In particular, the lines refer to $D_0 \approx 0.08$, 0.16, and $0.36L_z$. The spectra are normalized by multiplying by $\varepsilon^{-2/3}$.

Case	D_0/L_z	We_0	We_λ	Re_λ
1	–	–	–	145
2	0.36	0.5330	0.0220	83
3	0.16	0.8000	0.0776	101
4	0.08	2.0943	0.9339	111
5	0.36	2.0944	0.6773	113
6	0.16	4.0156	0.7536	117
7	0.08	10.4717	4.9313	132
8	0.36	4.1890	2.0103	122
9	0.16	7.9999	4.0868	131
10	0.08	20.9432	13.3057	142

TABLE 1. Summary of the DNS performed with different initial sizes of the interface D_0 and surface tension σ, all at a fixed Reynolds number $Re_z \approx 15000$ and volume fraction $\Phi = 5\%$.

investigated by others (Sekimoto *et al.* 2016). The resulting Taylor microscale Reynolds number at the steady state is equal to $Re_\lambda \approx 150$. The averaged spectrum of the TKE of this flow is reported in Figure 2(b). Owing to the high Reynolds number, a $k^{-5/3}$ regime develops at intermediate scales. As reported by Pumir (1996), the spectra of each individual component of the velocity are different at small wave numbers because of the large-scale anisotropy, while all spectra coincide at higher wave numbers. This difference is verified by our data [see Figure 2(b)].

We now consider the multiphase problem. After time $t \approx 100S^{-1}$, when the single-phase flow has already reached a statistically steady state, we inject spherical interfaces into the domain at random locations, globally enclosing a volume fraction of the suspended phase of 5%. The shape of all the interfaces is initially spherical with a fixed initial diameter D_0 in the inertial range of scale, as shown in Figure 2(b) with the vertical dashed lines. In particular, three different initial diameters are chosen, $D_0/L_z \approx 0.08$,

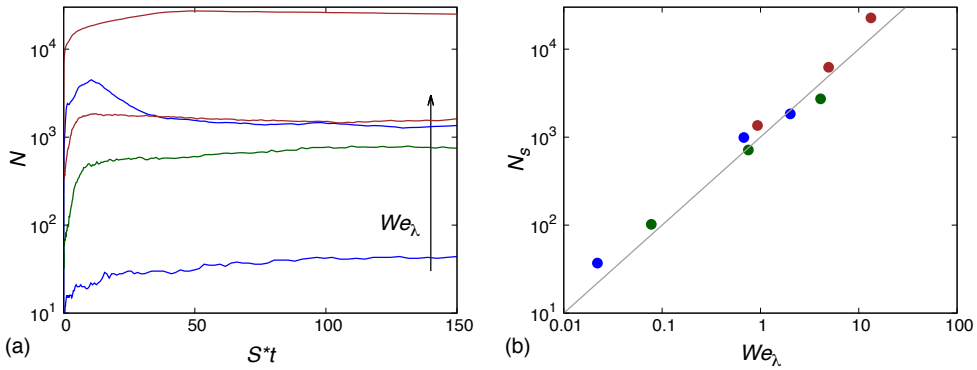

FIGURE 3. Number of interfaces $\mathcal{N}$ as a function of (a) time and (b) Weber number We_λ. Note that the scale of the vertical axis in the two figures is the same.

0.16, and 0.32, corresponding to 1.1, 2.5, and 5.6 of the single-phase Taylor microscale λ. After the introduction of the dispersed phase, a new short transient arises lasting approximately $50\mathcal{S}^{-1}$, eventually leading to a new statistically steady state, as depicted in Figure 2(a). The resulting Re_λ and We_λ are reported in Table 1. Clearly, the multiphase flows have lower Taylor microscale Reynolds numbers than the single-phase flow, and the difference decreases as the Weber number increases.

The above results demonstrate that stationarity is not unique to single-phase HST; it is also realizable in the presence of a second, dispersed phase. If permitted for a sufficient length of time, turbulent fluctuations can always reach equilibrium with a mean momentum flux, just as in the logarithmic region of turbulent boundary layers. Here, we define the stationary state in terms of the statistical properties of the flow averaged over both phases. Because the droplets can also break up or coalesce, it is natural to ask what steady-state size distributions they adopt and how that relates to the turbulence. These questions are answered in the following sections.

3.2. *Size distribution*

Figure 3 shows the temporal evolution of the number of droplets ($\mathcal{N}$) under various We_λ and initial sizes D_0. The counting is performed using a n-dimensional image processing library. Clearly, the droplet counts approach stable values for all the cases, consistent with the statistical stationary state measured by the averaged flow quantities. We note that $\mathcal{N}$ increases rapidly before $tS \approx 50$, suggesting that breakup is the dominant event during the period of energy growth. Eventually, turbulence dissipation increases and droplet breakup and coalescence tend to equilibrate. Plotting the steady-state value $\mathcal{N}_s$ as a function of We_λ, as in Figure 3(b), we observe that $\mathcal{N}_s$ is nearly linearly proportional to We_λ (a linear fit produces an exponent of approximately 1), independent of the initial size. Because a higher Weber number corresponds to lower surface energy, we conjecture that $\mathcal{N}_s$ will grow indefinitely with We_λ.

To further characterize the size distribution of the emulsion, we show the cumulative volume Vol as a function of the equivalent spherical diameter D in Figure 4(a). Each point on the curves represents the total volume of droplets with equivalent diameters less than D. Here, both Vol and D are normalized by the global maximal values so that the spectra are bounded uniformly from above. We observe that as the Weber number increases, the cumulative volume grows faster, indicating the presence of a larger proportion of small droplets, consistent with the increasing $\mathcal{N}_s$ noted above in Figure 3(a). The case with

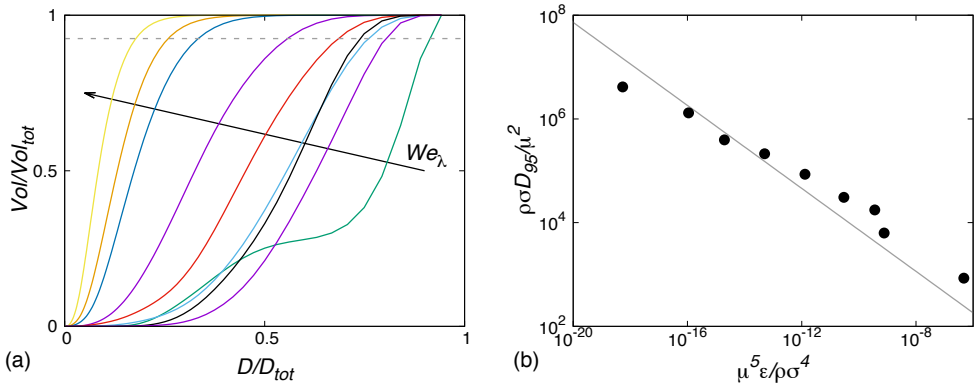

FIGURE 4. (a) Normalized cumulative volume distribution of the dispersed phase and (b) maximum droplet size as a function of the energy input. The grey solid line is the equation $\rho\sigma D_{95}/\mu^2 = 0.725\left(\mu^5\epsilon/\rho\sigma^4\right)^{-2/5}$.

the lowest We, however, exhibits a qualitatively different behavior that is still under investigation.

Another important parameter related to the size distribution is the largest droplet size D_{max}. Assuming breakup of droplets due to dynamic pressure forces, Hinze (1955) proposed that the largest possible droplet in a turbulent emulsifier is determined by the velocity fluctuation across D_{max}; if isotropy prevails and the scaling by Kolmogorov (1941) is accepted, dimensional analysis suggests $D_{max} \sim \varepsilon^{-2/5}$. Statistically, D_{max} can be approximated by the diameter of the droplet below which 95% of the total dispersed volume is occupied, i.e., $D_{max} \approx D_{95}$. Extracting D_{95} from our data and plotting it against the energy input, indeed we observe a $-2/5$ slope, see Figure 4(b). We note that, although Hinze developed his theory considering only isotropic turbulent flows dominated by the breakup process and neglecting the coalescence, he hypothesized that the same scaling law might still hold for nonisotropic flows provided that the droplet sizes fall within the inertial range. Inspection of the energy spectrum supports this argument. Our results suggest that the $-2/5$ scaling between the maximum droplet diameter and the turbulence dissipation applies not only to isotropic turbulence but also to the HST that we have analyzed.

3.3. *TKE budget*

The presence of the interface modifies the flow profoundly. The averaged spectrum of the TKE in the two-phase case is reported in Figure 2(b), where we observe that the interface mostly affects the large wave numbers (small scales) for which higher levels of energy are evident. At the same time, slightly lower energy is present at the large scales. Note that the result is analogous to what was already found for the case of decaying HIT for solid particles (Lucci *et al.* 2010) and bubbles (Dodd & Ferrante 2016); the increased energy at high wave numbers has been explained by the breakup of large eddies due to the presence of the suspension and the consequent creation of new eddies of smaller scale.

The TKE $\mathcal{K}$ is governed by the following equation

$$\frac{d\mathcal{K}}{dt} = \mathcal{P} - \varepsilon + \Psi_\sigma, \tag{3.1}$$

where the last term is the so-called power of surface tension first introduced by Dodd & Ferrante (2016). The equation can be easily obtained from the governing Navier–Stokes

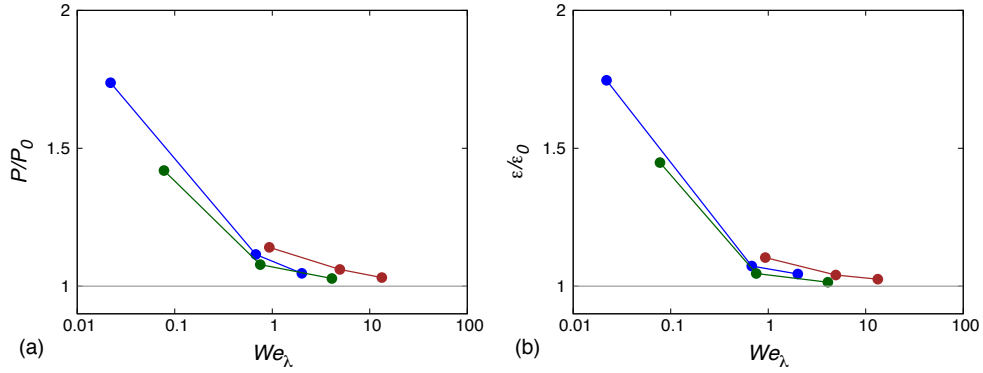

FIGURE 5. (a) Turbulent production $\mathcal{P}$ and (b) dissipation ε rates averaged over both phases as a function of the Weber number We, normalized by their value in the single-phase flow ($\mathcal{P}_0$ and ε_0).

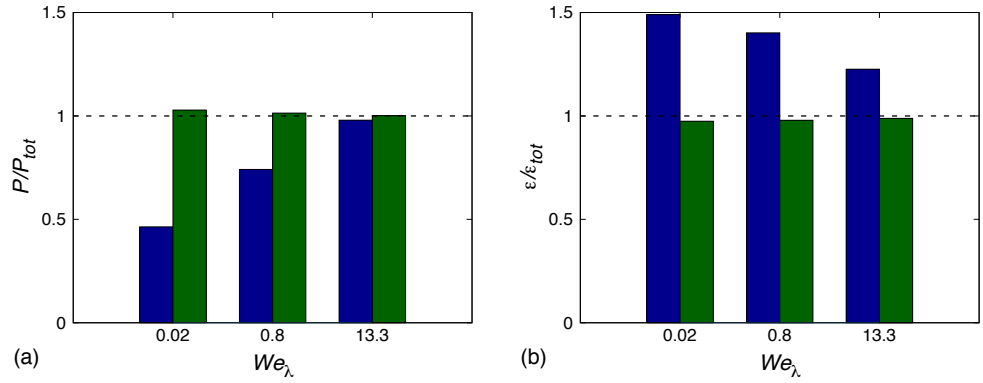

FIGURE 6. (a) Turbulent production $\mathcal{P}_m$ and (b) dissipation ε_m rates averaged over the two phases separately as a function of the Weber number We. The left and right columns are used to distinguish the dispersed and carrier phases, respectively.

equation [Eq. (2.1)] averaging over the whole volume and over both phases. At steady state, the rate of change of TKE is zero and the remaining terms are the production and dissipation rates and the power of surface tension. Figure 5 shows the production $\mathcal{P}$ and dissipation ε rates, normalized by their single-phase values, for all the simulations performed in the present study as a function of the Weber number We_λ. We observe that both the normalized production and dissipation rates are greater or equal to unity and decrease monotonically as the We_λ increases. Moreover, the two quantities have approximately the same value (the difference is less than 4%), thus indicating that at steady state the production balances the dissipation, similarly to a single-phase flow, and that the power of surface tension is on average zero. This result confirms the relation for Ψ_σ proposed by Dodd & Ferrante (2016), which relates the power of surface tension to the rate of change of surface area A, i.e., $\Psi_\sigma \sim -dA/dt$. Indeed, this relation implies that at steady state the rate of change of A is zero; thus, Ψ_σ is zero.

Equation (3.1) holds when averaging without distinguishing the two phases, but it is possible to obtain similar equations for the two phases separately. Indeed, by phase

averaging in one of the two fluids, we obtain

$$\frac{d\mathcal{K}_m}{dt} = \mathcal{P}_m - \varepsilon_m + \mathcal{T}_m^{\nu} + \mathcal{T}_m^{p} = \mathcal{P}_m - \varepsilon_m + \mathcal{T}_m, \tag{3.2}$$

where m is one of the two phases. The last two terms in the equation are related to the power of surface tension Ψ_σ (Dodd & Ferrante 2016); these are transport terms of TKE due to viscosity $\mathcal{T}_m^{\nu}$ and pressure $\mathcal{T}_m^{p}$, whose sum is $\mathcal{T}_m$. At steady state, the time derivative on the left-hand side is zero and the relation states that the production and dissipation are balanced by $\mathcal{T}_m$. Figure 6 shows histograms of the production $\mathcal{P}_m$ and dissipation ε_m rates as a function of the Weber number We_λ for three selected cases for the two phases. We observe that the production rate is lower in the dispersed phase than in the carrier phase, and the dissipation rate is higher in the dispersed fluid than in the carrier fluid. These results indicate that the transport term $\mathcal{T}_m$ is positive in the dispersed fluid and negative in the carrier, corresponding to a TKE transfer from the carrier to the dispersed phase; i.e., the presence of the droplets is overall a sink for the TKE of the bulk fluid. In addition, we observe that the difference in $\mathcal{P}_m$ and ε_m decreases with We_λ.

4. Conclusions

We have simulated a two-phase HST flow at $Re_z \approx 15000$. The droplets are initially spheres providing 5% volume fraction of the suspended phase. We showed that the two-phase flow is able to reach a statistically steady state in terms of both TKE and droplet number and size. The resulting flow has a lower Reynolds number based on the Taylor microscale than the single-phase flow does; this is due to the presence of the interface, which results in increased production and dissipation rates of TKE. We have showed that the surface tension power has no effect on average, because production and dissipation are statistically in balance. We have also proved that the interface acts as a sink of TKE for the carrier phase, with a net flux going from the bulk of the fluid to the dispersed phase, where it is dissipated.

Acknowledgments

The authors acknowledge computer time provided by the Swedish National Infrastructure for Computing and by the National Infrastructure for High Performance Computing and Data Storage in Norway. The authors also acknowledge use of computational resources from the Certainty cluster awarded by the National Science Foundation to CTR.

REFERENCES

Balachandar, S. & Eaton, J. K. 2010 Turbulent dispersed multiphase flow. *Annu. Rev. Fluid Mech.* **42**, 111–133.

Brackbill, J. U., Kothe, D. B. & Zemach, C. 1992 A continuum method for modeling surface tension. *J. Comput. Phys.* **100**, 335–354.

Cate, A. T., Derksen, J. J., Portela, L. M. & Van Den Akker, H. E. A. 2004 Fully resolved simulations of colliding monodisperse spheres in forced isotropic turbulence. *J. Fluid Mech.* **519**, 233–271.

Dodd, M. S. & Ferrante, A. 2016 On the interaction of Taylor length scale size droplets and isotropic turbulence. *J. Fluid Mech.* **806**, 356–412.

Eaton, J. K. & Fessler, J. R. 1994 Preferential concentration of particles by turbulence. *Int. J. Multiphase Flow. Flow* **20**, 169–209.

Ferrante, A. & Elghobashi, S. 2003 On the physical mechanisms of two-way coupling in particle-laden isotropic turbulence. *Phys. Fluids* **15**, 315–329.

Gerz, T., Schumann, U. & Elghobashi, S. E. 1989 Direct numerical simulation of stratified homogeneous turbulent shear flows. *J. Fluid Mech.* **200**, 563–594.

Hinze, J. O. 1955 Fundamentals of the hydrodynamic mechanism of splitting in dispersion processes. *AIChE J.* **1**, 289–295.

Ii, S., Sugiyama, K., Takeuchi, S., Takagi, S., Matsumoto, Y. & Xiao, F. 2012 An interface capturing method with a continuous function: the THINC method with multi-dimensional reconstruction. *J. Comput. Phys.* **231**, 2328–2358.

Kolmogorov, A. N. 1941 The local structure of turbulence in incompressible viscous fluid for very large Reynolds numbers. *Dokl. Akad. Nauk* **30**, 299–303.

Lee, M. J., Kim, J. & Moin, P. 1990 Structure of turbulence at high shear rate. *J. Fluid Mech.* **216**, 561–583.

Lucci, F., Ferrante, A. & Elghobashi, S. 2010 Modulation of isotropic turbulence by particles of Taylor length-scale size. *J. Fluid Mech.* **650**, 5–55.

Picano, F., Breugem, W. P. & Brandt, L. 2015 Turbulent channel flow of dense suspensions of neutrally buoyant spheres. *J. Fluid Mech.* **764**, 463–487.

Pumir, A. 1996 Turbulence in homogeneous shear flows. *Phys. Fluids* **8**, 3112–3127.

Rogers, M. & Moin, P. 1987 The structure of the vorticity field in homogeneous turbulent flows. *J. Fluid Mech.* **176**, 33–66.

Rosti, M. E., De Vita, F. & Brandt, L. 2018 Numerical simulations of emulsions in shear flows. *Acta Mech.* https://doi.org/10.1007/s00707-018-2265-5.

Sardina, G., Schlatter, P., Brandt, L., Picano, F. & Casciola, C. M. 2012 Wall accumulation and spatial localization in particle-laden wall flows. *J. Fluid Mech.* **699**, 50–78.

Sekimoto, A., Dong, S. & Jiménez, J. 2016 Direct numerical simulation of statistically stationary and homogeneous shear turbulence and its relation to other shear flows. *Phys. Fluids* **28**, 035101.

Sukheswalla, P., Vaithianathan, T. & Collins, T. 2013 Simulation of homogeneous turbulent shear flows at higher Reynolds numbers: numerical challenges and a remedy. *J. Turbul.* **14**, 60–97.

Tanaka, M. 2017 Effect of gravity on the development of homogeneous shear turbulence laden with finite-size particles. *J. Turbul.* **18**, 1144–1179.

Tavoularis, S. & Corrsin, S. 1981*a* Experiments in nearly homogeneous turbulent shear flow with a uniform mean temperature gradient. Part 2. The fine structure. *J. Fluid Mech.* **104**, 349–367.

Tavoularis, S. & Corrsin, S. 1981*b* Experiments in nearly homogenous turbulent shear flow with a uniform mean temperature gradient. Part 1. *J. Fluid Mech.* **104**, 311–347.

Tryggvason, G., Sussman, M. & Hussaini, M. Y. 2007 Immersed boundary methods for fluid interfaces. In Prosperetti, A. & Tryggvason, G. (Eds.) *Computational Methods for Multiphase Flow*. Cambridge University Press.

Youngs, D. L. 1982 Time-dependent multi-material flow with large fluid distortion. In Morton, K. W. & Baines M. J. (Eds.) *Numerical methods for fluid dynamics*. Academic Press.